frontiers | Frontiers in Chemistry

TYPE Original Research
PUBLISHED 26 September 2022
DOI 10.3389/fchem.2022.954588

OPEN ACCESS

EDITED BY
Porun Liu,
Griffith University, Australia

REVIEWED BY
Iver Lauermann,
Helmholtz Association of German Research Centers (HZ), Germany
Jincheng Fan,
Changsha University of Science and Technology, China

*CORRESPONDENCE
Yongtao Qu,
y.qu@northumbria.ac.uk
Vincent Barrioz,
vincent.barrioz@northumbria.ac.uk

SPECIALTY SECTION
This article was submitted to Electrochemistry, a section of the journal Frontiers in Chemistry

RECEIVED 27 May 2022
ACCEPTED 19 August 2022
PUBLISHED 26 September 2022

CITATION
Campbell S, Phillips LJ, Major JD, Hutter OS, Voyce R, Qu Y, Beattie NS, Zoppi G and Barrioz V (2022), Routes to increase performance for antimony selenide solar cells using inorganic hole transport layers.
Front. Chem. 10:954588.
doi: 10.3389/fchem.2022.954588

Routes to increase performance for antimony selenide solar cells using inorganic hole transport layers

Stephen Campbell[1], Laurie J. Phillips[2], Jonathan D. Major[2], Oliver S. Hutter[1], Ryan Voyce[1], Yongtao Qu[1]*, Neil S. Beattie[1], Guillaume Zoppi[1] and Vincent Barrioz[1]*

[1]Department of Mathematics, Physics and Electrical Engineering, Northumbria University, Newcastle Upon Tyne, United Kingdom, [2]Department of Physics, University of Liverpool, Liverpool, United Kingdom

Simple compound antimony selenide (Sb_2Se_3) is a promising emergent light absorber for photovoltaic applications benefiting from its outstanding photoelectric properties. Antimony selenide thin film solar cells however, are limited by low open circuit voltage due to carrier recombination at the metallic back contact interface. In this work, solar cell capacitance simulator (SCAPS) is used to interpret the effect of hole transport layers (HTL), i.e., transition metal oxides NiO and MoO_x thin films on Sb_2Se_3 device characteristics. This reveals the critical role of NiO and MoO_x in altering the energy band alignment and increasing device performance by the introduction of a high energy barrier to electrons at the rear absorber/metal interface. Close-space sublimation (CSS) and thermal evaporation (TE) techniques are applied to deposit Sb_2Se_3 layers in both substrate and superstrate thin film solar cells with NiO and MoO_x HTLs incorporated into the device structure. The effect of the HTLs on Sb_2Se_3 crystallinity and solar cell performance is comprehensively studied. In superstrate device configuration, CSS-based Sb_2Se_3 solar cells with NiO HTL showed average improvements in open circuit voltage, short circuit current density and power conversion efficiency of 12%, 41%, and 42%, respectively, over the standard devices. Similarly, using a NiO HTL in TE-based Sb_2Se_3 devices improved open circuit voltage, short circuit current density and power conversion efficiency by 39%, 68%, and 92%, respectively.

KEYWORDS

Sb_2 Se_3, photovoltaic, inorganic hole transport layers, SCAPs, thin films

1 Introduction

Antimony selenide (Sb_2Se_3), as a simple and low-cost compound with a direct energy band gap (~1.18 eV), high absorption coefficient ($> 10^5$ cm^{-1}) and high carrier mobility (~10 cm^2/Vs, is a promising emergent light absorber for photovoltaic (PV) applications (Chen et al., 2015; Chen et al., 2017; Birkett et al., 2018). As a material, Sb_2Se_3 is mainly

composed of $(Sb_4Se_6)_n$ as 1-D ribbon structures, where the ribbons are strongly coupled by covalent bonds running along the c-axis with weaker Van der Waals (VdW) interactions between the ribbons. Thus, stacking of the ribbons occurs due to the weaker VdW bonds (Deringer et al., 2015). Hole mobility is enhanced in the *c*-axis and can reach 45 cm^2/Vs along the ribbons (Black et al., 1957).

A number of studies have reported that Sb_2Se_3 thin films with preferred crystallographic orientation along the (*hk*1) direction, particularly (221), resulted in devices with higher efficiencies (Leng et al., 2014; Yuan et al., 2016; Li et al., 2017). The improved performance is often attributed to increased charge transport through the (*hk*1)-oriented ribbons perpendicular to the substrate and benign grain boundaries in this material (Chen et al., 2017; Williams et al., 2020). Wang and co-workers demonstrated the dependence of Sb_2Se_3 PV device performance on the preferred crystal orientation of the absorber (Wang et al., 2017). In that work, by optimising growth conditions, Sb_2Se_3 solar cells with preferred (211) and (221)-orientations on CdS and ZnO achieved higher efficiencies (5.6% and 6.0%, respectively) than those with (020) and (120)-orientations (3.2% and 4.8%, respectively). For planar Sb_2Se_3 solar cells in substrate orientation, a record efficiency of 6.5% has been reported with the $Cd_{0.75}Zn_{0.25}S$ buffer layer being used as an alternative to CdS (Figure 1A shows standard substrate device). Meanwhile, Sb_2Se_3 devices with this buffer layer but in a superstrate structure (Figure 1B) have achieved an efficiency of 7.6% (Wen et al., 2018). Recently, a record substrate device efficiency of 9.2% was obtained by growing (001)-oriented Sb_2Se_3 nanorod arrays on sputtered molybdenum layers (Li et al., 2019). A conformal interfacial TiO_2 layer was used to mitigate the migration of elemental antimony (Sb) into the CdS buffer layer, as interdiffusion has been shown to create a detrimental CdSe interlayer (Phillips et al., 2019).

In this work, thin transition metal oxides, NiO and MoO_x, are applied as HTLs in substrate Sb_2Se_3 devices to improve carrier selectivity at the back electrode by controlling inter-diffusion and formation of secondary phase materials (such as $MoSe_2$) at the interface. Additionally, NiO and MoO_x HTLs are deposited on superstrate Sb_2Se_3 films before making Au back contacts to alter the energy band alignments at the back contact effectively producing an electron reflector, and minimising carrier recombination.

In the first part of this study, Sb_2Se_3 substrate/superstrate device simulations using solar cell capacitance simulator (SCAPS) are conducted in order to interpret the effect of HTLs on Sb_2Se_3 device characteristics (Burgelman et al., 2000). We then characterise the material properties of MoO_x and NiO thin films deposited at room temperature by electron beam evaporation. At this temperature it was found that NiO formed a crystalline film, unlike MoO_x which was amorphous. Sb_2Se_3 absorber films were then fabricated by close-space sublimation (CSS) and thermal evaporation (TE) techniques and incorporated into superstrate and substrate solar cell configurations. HTLs were inserted at the metal electrode/Sb_2Se_3 absorber interface and their effect on Sb_2Se_3 crystallinity and solar cell performance is comprehensively studied.

2 Experimental section

2.1 Device fabrication

The basic structure of substrate Sb_2Se_3 solar cells was as follows: Soda lime glass (SLG)/Mo/Sb_2Se_3/CdS/ZnO/ITO/Ni-Al. Mo coated soda lime glass (SLG) substrates measuring 7.5 cm^2 × 2.5 cm^2 were used in this study. NiO or MoO_x HTLs were deposited between the Mo electrode and Sb_2Se_3. Thin HTL films of 15 nm thickness were deposited using e-beam evaporation. 500 nm thick Sb_2Se_3 layers were prepared by TE of crystalline/powder Sb_2Se_3 source material (Alfa Aesar, 99.99%) at a deposition rate of ~15 Å/s. The substrates were maintained at a temperature of 300°C throughout the deposition. The Sb_2Se_3 films were subsequently subjected to a heat treatment

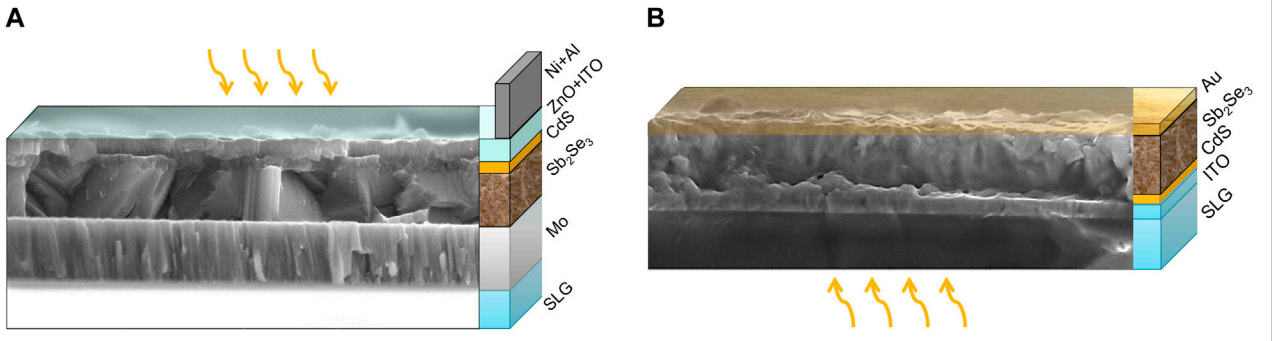

FIGURE 1
Standard planar **(A)** substrate and **(B)** superstrate configuration Sb_2Se_3 solar cells.

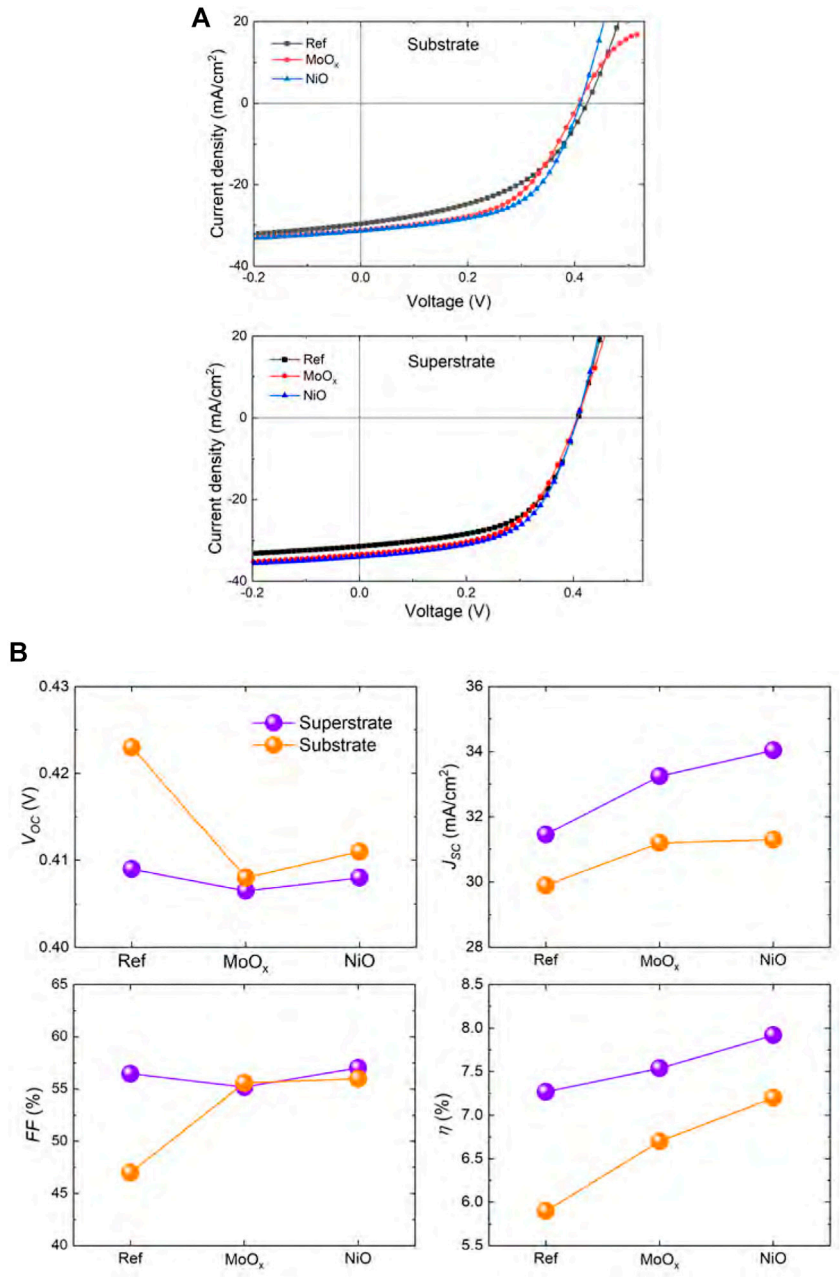

FIGURE 2
(A) *J-V* curves and **(B)** *J-V* parameters of simulated Sb_2Se_3 solar cells with different HTL materials. Roll-over behaviour is observed in the *J-V* curve of substrate devices with MoO_x HTL.

at 300°C for 30 min in Ar atmosphere in a tube furnace to promote recrystallisation. For the CSS Sb_2Se_3 films, a compact seed layer was grown at 0.05 mbar N_2 for 5 min with a source temperature of 350°C, followed by a 30 min growth step at 13 mbar and a source temperature of 450°C to produce a compact and highly orientated grain structure. The substrate was then rapidly cooled with N_2. An *n*-type CdS buffer layer (~60 nm) was deposited by chemical bath deposition followed by DC-pulsed sputtering deposition of an *i*-ZnO (~35 nm) layer plus a transparent conductive window layer ITO (~200 nm). Front contact grids comprising Ni (~50 nm) and Al (~1,000 nm) were deposited through a shadow mask by e-beam evaporation. Finally, 0.16 cm^2 cells were defined by mechanical scribing on each substrate.

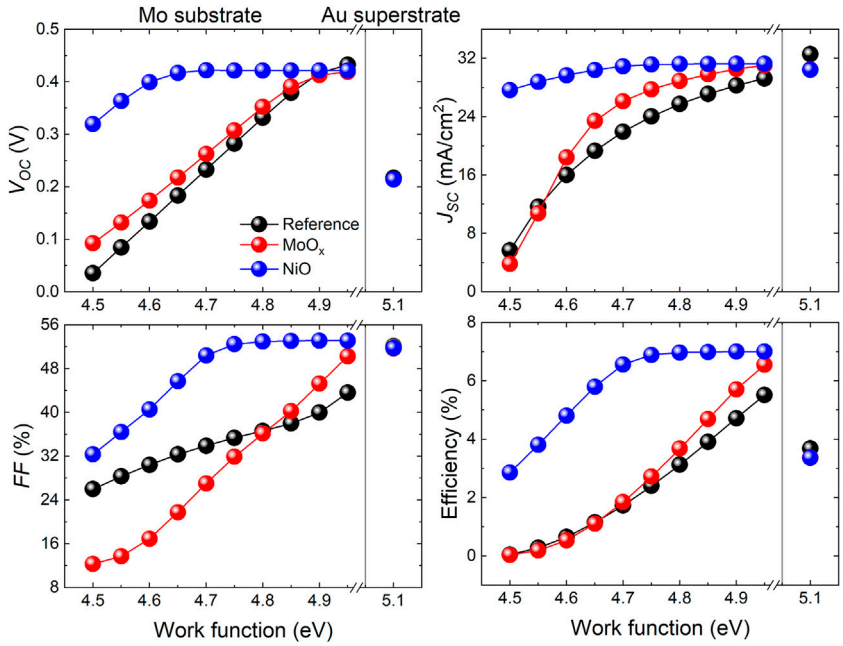

FIGURE 3
J-V parameters of simulated Sb_2Se_3 substrate devices with Mo back contact (varying Mo WF between 4.50–4.95 eV) and simulated Sb_2Se_3 superstrate devices with Au back contact (WF at 5.1 eV).

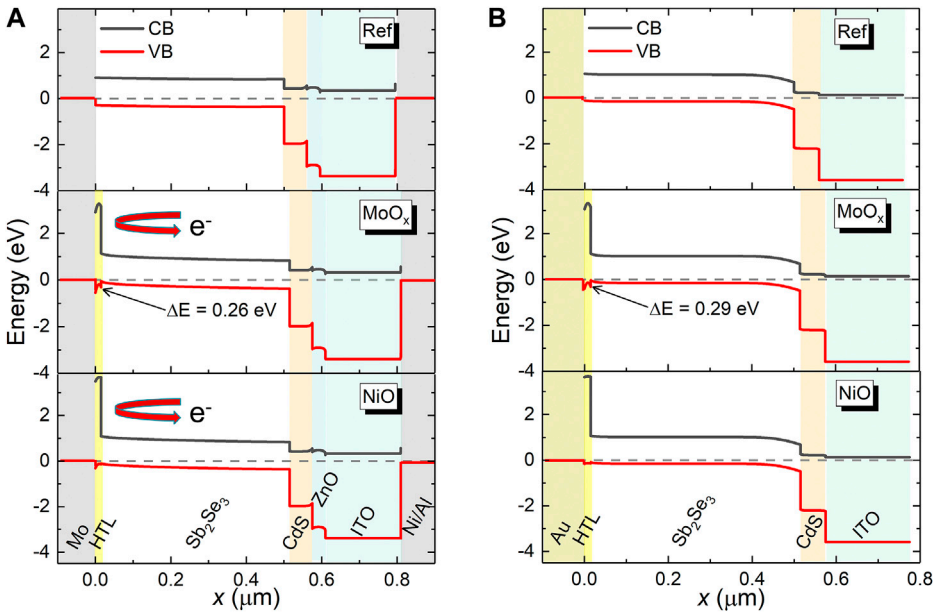

FIGURE 4
Energy level alignment for the devices in substrate **(A)** and superstrate **(B)** orientati1ons. Devices without a hole transport layer (top), with a MoO_x layer (middle) and a NiO layer (bottom) are shown.

Superstrate Sb_2Se_3 solar cells have the following configuration: SLG/ITO/CdS/Sb_2Se_3/Au with NiO or MoO_x HTLs deposited between the metal contact and Sb_2Se_3 absorber. The ITO layer was deposited by DC-pulsed sputtering and Sb_2Se_3 layers were grown by TE and CSS as detailed above. Finally, Au back contacts with an area of 0.07 cm^2 were deposited through a shadow mask by e-beam evaporation.

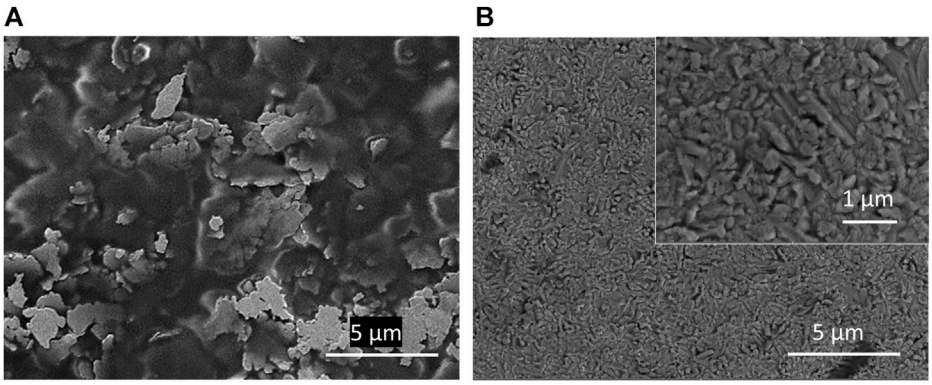

FIGURE 5
Top-down SEM image of a 100 nm **(A)** MoO_x film and **(B)** NiO films on glass. Inset: Higher magnification image of the NiO film, showing the nanostructure.

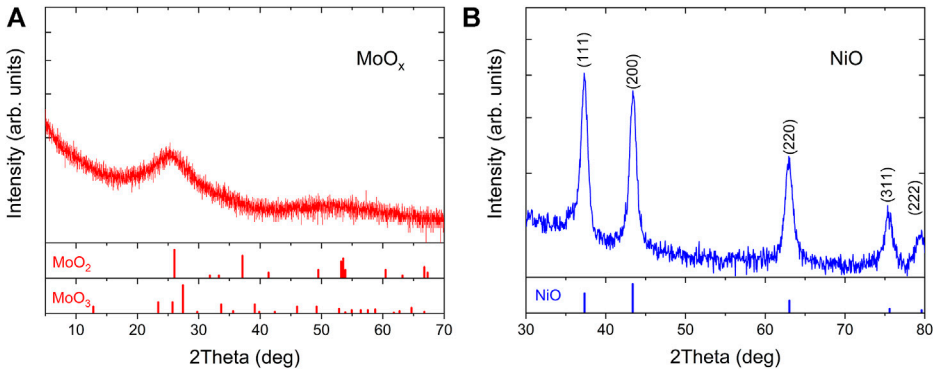

FIGURE 6
XRD pattern of 100 nm films of **(A)** MoOx and **(B)** NiO on soda lime glass (SLG). Reference XRD data for MoO_2, MoO_3 and NiO are shown underneath the XRD with JPDCS card ID 65-5787, 35-0609 and 04-0,835 respectively.

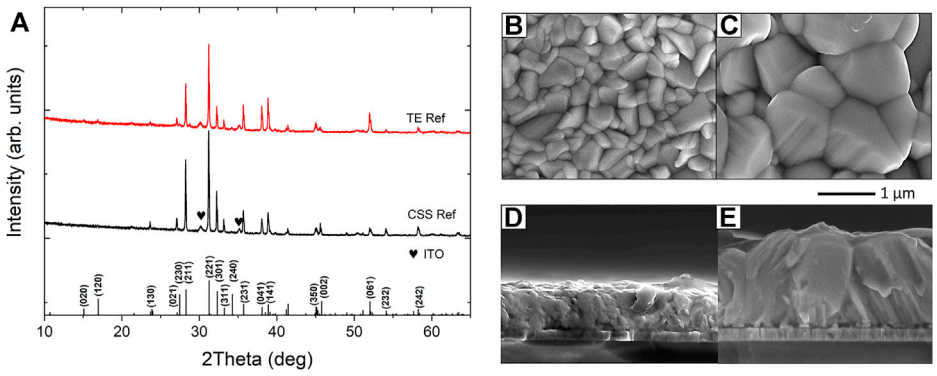

FIGURE 7
(A) XRD patterns of Sb_2Se_3 layers deposited by TE and CSS on ITO/CdS superstrates with standard diffraction pattern for Sb_2Se_3 (JCPDS15-0861) included for reference and SEM images of corresponding TE **(B,D)** and CSS **(C,E)** Sb_2Se_3 samples.

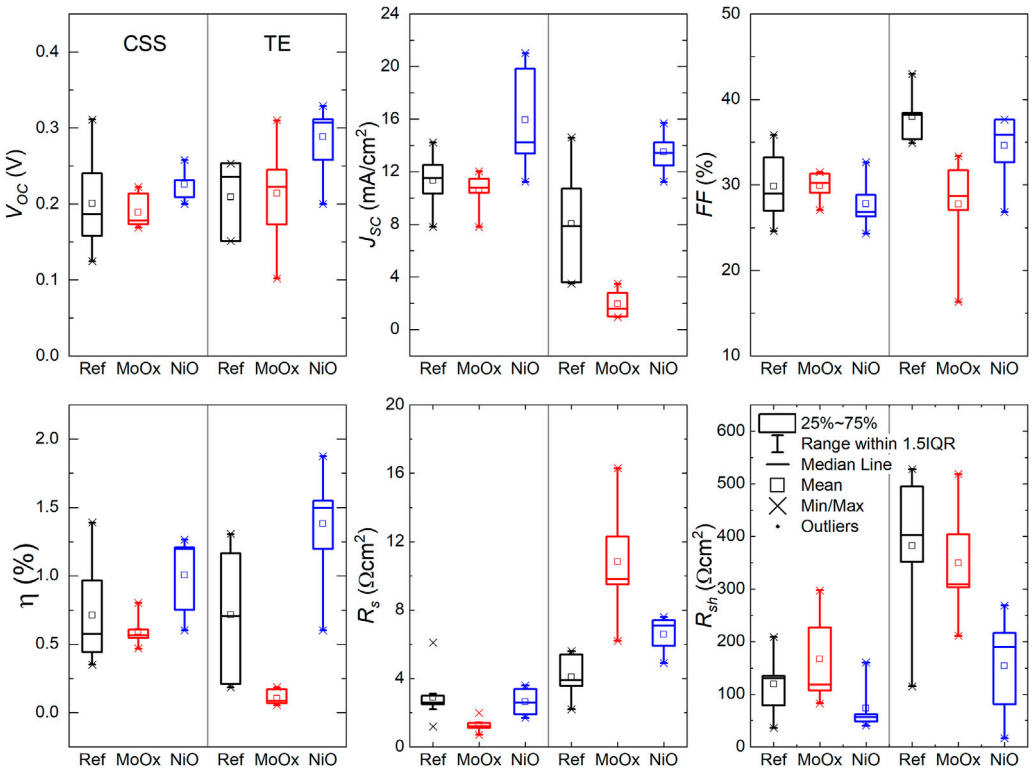

FIGURE 8
J-V parameters of superstrate TE and CSS Sb_2Se_3 devices with incorporated MoO_x and NiO HTLs. □ is the average value and × is the minimum and maximum position. The three horizontal lines of each box stand for the 25%, 50%, and 75% of the reading distribution. The whisker range is determined by the standard deviation of the sampled devices. IQR is the inter-quartile range.

2.2 Material and device characterisation

The crystal structures of Sb_2Se_3 were characterised by X-ray diffraction (XRD) with Cu Kα1 (1.54056 Å) radiation (Rigaku SmartLab SE). The surface morphology and cross-sectional images of Sb_2Se_3 films were taken by scanning electron microscopy (SEM, Tescan Mira 3 FEG-SEM). Optical spectroscopy measurements were performed using a Shimadzu UV-2600 spectrophotometer fitted with an integrating sphere. Kelvin probe force microscopy (KFPM) measurements were done using a KP Technology KP020 single point kelvin probe system fitted with a standard 2 mm Au tip.

Current-density vs. voltage (*J-V*) measurements of Sb_2Se_3 thin film solar cells were performed using an Abet Technologies solar simulator at 1-sun (100 mW/cm^2) illumination equivalent to air mass 1.5 global spectrum with light power density calibrated using a Si reference cell.

2.3 Device simulation

Device simulation was carried out for both substrate and superstrate configuration Sb_2Se_3 solar cell using Solar Cell Capacitance Simulator (SCAPS 1-D), which is based on the solutions to Poisson's equation and continuity equation for electrons and holes in the vertical heterostructure of multilayer thin film PV device (Burgelman et al., 2000). The input parameters of the solar cells were defined with the Sb_2Se_3, HTL and electron transport layer (ETL) semiconducting properties, including experimentally determined bandgaps, electron affinity, density of states (Zeng et al., 2016), mobility of charge carriers (Chen et al., 2017), acceptor/donor concentrations (Wang et al., 2015), and defect state density (Leijtens et al., 2016). Defects were introduced at the Sb_2Se_3/CdS interface to simulate realistic device performance.

3 Results and discussion

3.1 Simulated Sb_2Se_3 devices

Simulation analysis using SCAPS software was implemented to evaluate the performance of reference substrate and superstrate Sb_2Se_3 solar cells and those incorporating MoO_x and NiO as HTLs, subsequently

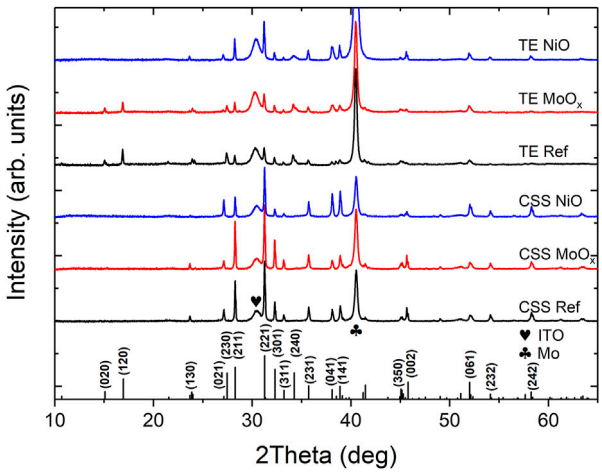

FIGURE 9
XRD patterns of Sb_2Se_3 films deposited by TE or CSS on top of NiO, MoO_x and Mo-coated SLG.

referred to as samples Ref, MoO_x and NiO, respectively (see Table 1 for film properties). Figure 2 shows the *J-V* curves and corresponding box plots of *J-V* parameters of both Sb_2Se_3 device configurations with incorporated HTLs. Regarding the substrate devices, all device parameters are improved, with the exception of V_{oc} which shows a slight decrease for devices with a HTL (down from 0.423 V for the reference device to 0.408 and 0.411 V for MoO_x and NiO devices, respectively). However, devices with MoO_x HTL show evidence of roll-over behaviour. The roll-over phenomenon, which occurs near the V_{oc} in a light *J-V* curve, is due to Schottky energy barrier formed at the absorber/metal interface at a solar cell back contact (Eisenbarth et al., 2011; Hädrich et al., 2011). It acts as a reverse biased diode when the main junction is forward biased, blocking carrier transport for increasing forward bias, resulting in roll-over behaviour in light *J-V* characteristics. The baseline J_{sc} in the reference device was 29.9 mA/cm^2, rising to 31.2 and 31.3 mA/cm^2 in MoO_x and NiO devices, respectively. Addition of HTL films to the reference device demonstrated a notable increase in *FF* for substrate devices. The *FF* in the reference device was 47.0%, rising to a maximum of 55.6% and 56.0% in the MoO_x and NiO devices, respectively. The increase in J_{sc} and *FF* of devices with integrated HTL materials directly translates into improvements in power conversion efficiency, PCE [η = 5.9% (Ref), 6.7% (MoO_x) and 7.2% (NiO)]. The current-blocking energy barrier at the back contact of the MoO_x substrate device could explain the lower PCE in comparison to the device with a NiO HTL. It is important to note that the results shown are not representative of the maximum conversion efficiencies that may be achieved with Sb_2Se_3, as we are focusing solely on the effect of the HTL, while using currently available materials parameters.

For superstrate Sb_2Se_3 solar cells, devices with an incorporated HTL showed an increase in J_{sc} of around 8% from 31.5 mA/cm^2 observed in the reference device to 33.5 and 34.0 mA/cm^2 in the devices with a MoO_x and NiO HTL, respectively. As a result of the improvement in J_{sc}, the PCE of solar cells with a HTL increased to 7.5% (MoO_x) and 8.0% (NiO) from the reference value of 7.3%. Interestingly, no roll-over was seen in the *J-V* curve for the MoO_x device which could be related to the use of Au as metallic back contact rather than Mo in the substrate devices. The work function (WF) of a metal employed as a rear contact on a PV device plays an important role in facilitating hole extraction at the contact (Fleck et al., 2020). Typically, Au is reported to have a WF of 5.10 eV (Michaelson, 1977) and Mo has WFs ranging from 4.50–4.95 eV, depending on the preferred crystal orientation of the metal (Green, 1969; Michaelson, 1977; Hölzl and Schulte, 1979). To illustrate the effect of back contact metal WF on substrate/superstrate Sb_2Se_3 device performance, Figure 3 shows the dependence of *J-V* parameters on the WF of Mo and Au metals. It is apparent that the J-V parameters of all substrate devices are sensitive to variations in the value of Mo WF. In the Ref and MoO_x substrate devices, V_{oc} decreases monotonically with Mo WF where a significant drop is observed from 0.432 V to 0.422 V at WF 4.95 eV to 0.036 V and 0.093 V at WF 4.50 eV for Ref and MoO_x devices, respectively. This is a clear indication of an increasing back contact barrier with decreasing Mo WF. This phenomenon has been observed experimentally in Sb_2Se_3 solar cells previously (Liu et al., 2014; Li et al., 2017). The V_{oc} in the NiO device is less affected by the Mo WF, reducing from 0.422 V at WF 4.95 eV to 0.319 V at WF 4.50 eV. A similar trend is seen in J_{sc}, *FF* and η parameters for the substrate devices. However, a low Mo WF of 4.50 eV causes a notable decrease in *FF* of the MoO_x device (12.3%), compared to the Ref and NiO devices (26.0% and 32.4%).

In order to understand the improvement of the device performance with the introduction of HTLs, it is necessary to consider the energy band alignment at the interfaces at the back of the PV devices. Figure 4 shows the simulated energy band diagrams of substrate and superstrate Sb_2Se_3 devices incorporating NiO and MoO_x HTLs. Due to a small electron affinity (EA = 1.46 eV (NiO), 2.05 eV (MoO_x)) and large band gaps (E_g ~3.80 eV (NiO), 3.50 eV MoO_xx)) in both HTL materials, a large potential energy barrier is formed at the back contact, reflecting electrons. This barrier minimises carrier recombination at the back interfaces with Sb_2Se_3 and improves conductivity at the back electrode. However, it is apparent that a non-negligible hole barrier of 0.26 and 0.29 eV is formed at the MoO_x/Sb_2Se_3 interface of the substrate and superstrate devices, respectively, which can manifest as *J-V* roll-over behaviour seen in the simulated MoO_x substrate device. Thus the SCAPS simulations indicate the incorporation of a MoO_x or NiO HTL into substrate and superstrate configuration Sb_2Se_3 solar cells increases device performance compared to a standard solar cell by the introduction of a high energy barrier to electrons at the rear absorber/metal interface.

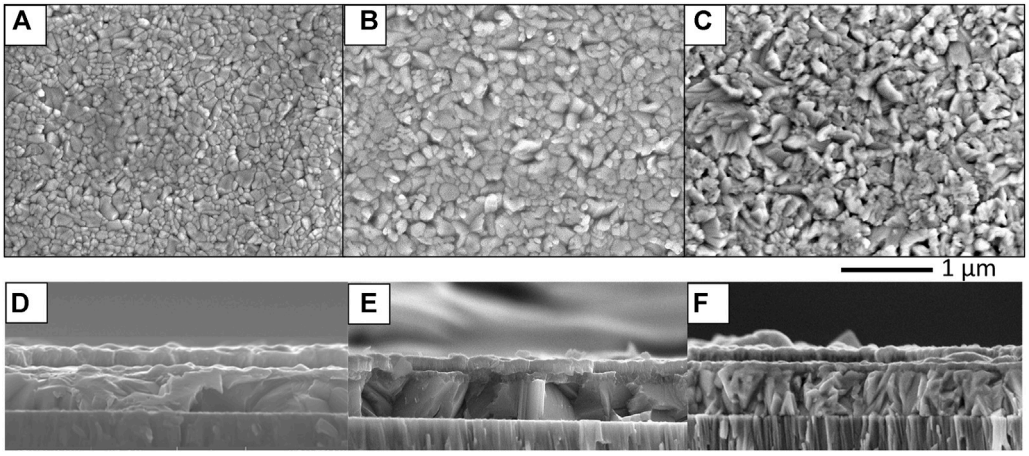

FIGURE 10
Top-down and cross-sectional SEM images of reference substrate **(A,D)**, MoO_x **(B,E)** and NiO **(C,F)** of Sb_2Se_3 films deposited by thermal evaporation.

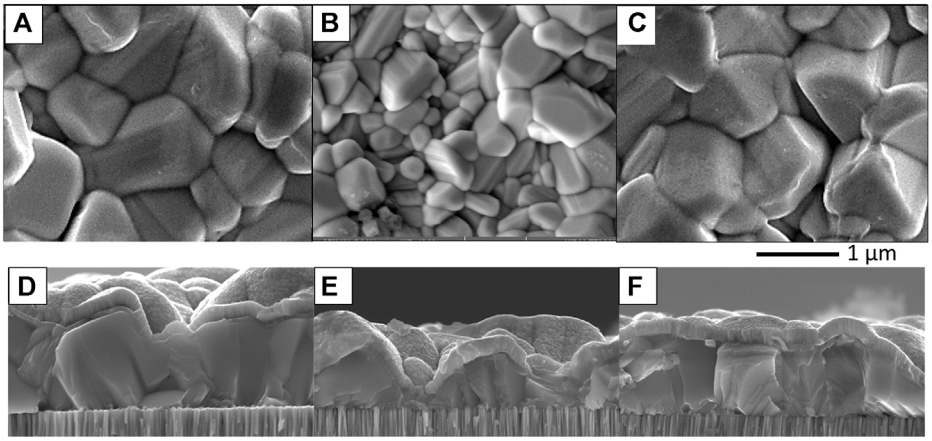

FIGURE 11
Top-down and cross-sectional SEM images of reference substrate **(A,D)**, MoO_x **(B,E)** and NiO **(C,F)** of Sb_2Se_3 films deposited by close-space sublimation.

3.2 Fabricated Sb_2Se_3 devices

100 nm thick films of MoO_x and NiO were deposited on SLG at room temperature to facilitate characterisation of the HTLs. Figure 5 shows surface morphology SEM images of the respective HTLs. The MoO_x film exhibits an amorphous, flake-like structure in comparison to a compact crystalline morphology observed in the NiO film. XRD patterns in Figure 6 confirm the amorphous and crystalline nature of the MoO_x and NiO films, respectively. All the diffraction peaks in the NiO thin film were identified and indexed to cubic NiO (JCPDS number 04-0835) and no diffraction peaks of other impurity phases were observed.

Supplementary Materials S1A shows the spectral transmittance and reflectance of the NiO and MoO_x films on SLG. Both HTLs are highly transparent in the visible and near-infrared wavelength region and their transmittance falls sharply at ultraviolet wavelengths. However, the amorphous MoO_x film has slightly lower transmittance/higher reflectance in the sub-600 nm wavelength region compared to the crystalline NiO film. The bandgap energy (E_g) of the HTL films was calculated by extrapolation of the linear region of the Tauc plot to the x-axis, according to the relation (Tauc et al., 1966):

$$(\alpha h\nu)^2 = A\left(h\nu - E_g\right) \quad (1)$$

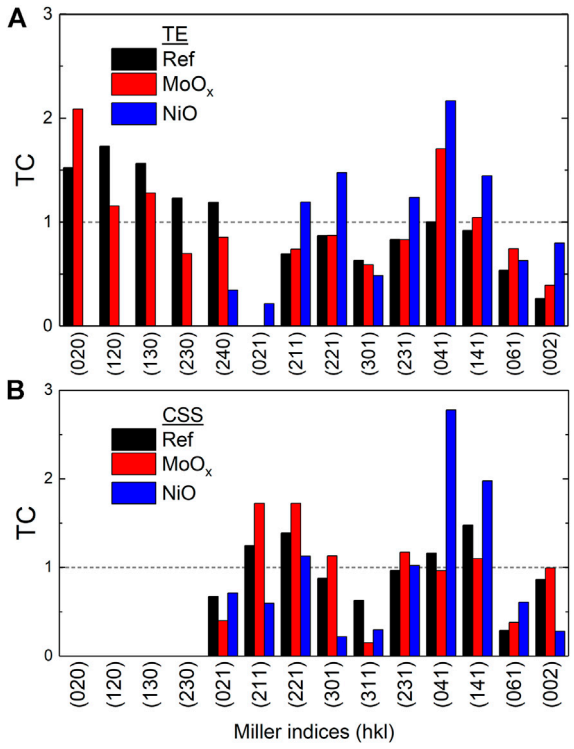

FIGURE 12
Texture coefficient analysis from XRD patterns of Sb_2Se_3 films deposited *via* TE **(A)** and CSS **(B)** with different hole transport layers in substrate configuration. A diffraction peak with a relatively large TC value (>1) indicates a preferred orientation of the grain along this direction.

where α is the absorption coefficient of the semiconductor material, h is Planck's constant, ν is the frequency of the electromagnetic radiation and A is a constant of proportionality. The estimated E_g values of NiO and MoO_x films are 3.95 and 3.85 eV, respectively (see Supplementary Materials S1B). A HTL film thickness of 15 nm was incorporated into the superstrate/substrate device to ensure a conformal coating of the HTL. A HTL requires a thickness sufficient to preserve the desired material properties and not impede charge transport considerably which would detrimentally increase series resistance in the finished devices.

3.3 Superstrate devices

TE and CSS deposition techniques were employed for Sb_2Se_3 film growth on SLG/ITO/CdS superstrates. For TE, the SLG/ITO/CdS superstrates were heated to 300°C prior to Sb_2Se_3 deposition in order to promote the growth of preferred ($hk1$) crystal orientations while minimising ($hk0$) orientations (Zhou et al., 2015) ($hk0$) planes, specifically (120), have been found to be detrimental to carrier transport (Guo et al., 2018; Wen et al., 2018; Li et al., 2019). The ($hk0$)-oriented Sb_2Se_3 nanoribbons are stacked parallel to the ITO/SLG superstrate where conductivity is inhibited by electrically insulating VdW bonds between the stacked nanoribbons. A seed layer is used in Sb_2Se_3 films deposited *via* CSS. This seed layer has a high density of nucleation points for the second stage of growth during the CSS process, which improves uniformity, raising the average efficiency of devices (Hutter et al., 2018a). Transmittance and reflectance data for a representative TE Sb_2Se_3 film was used to determine the E_g from a Tauc plot, which gave a E_g value of 1.17 eV in good agreement with (Birkett et al., 2018), see Supplementary Materials S2A,B. XRD patterns for Sb_2Se_3 films deposited by TE and CSS are shown in Figure 7A. The peaks in both XRD patterns are sharp and well resolved indicating the polycrystalline nature of the Sb_2Se_3 thin films. The lattice planes are cross-referenced to JCPDS card no. 15-0861 confirming the formation of orthorhombic Sb_2Se_3 with space group Pbnm. Both XRD patterns show similar characteristics, exhibiting strong (211) and (221) peaks with minimal contributions from ($hk0$) planes. Figures 7B–E shows the top and cross-sectional SEM images of Sb_2Se_3 thin films deposited by TE and CSS. The different growth techniques result in contrasting Sb_2Se_3 film morphologies. TE produces Sb_2Se_3 films of uniform thickness of ~500 nm and densely packed grains, confirming the good crystallinity of the films, consistent with the XRD results (Figures 7B,D). However, this deposition method did not form a conformal coating of the Sb_2Se_3 film across the entire superstrate with the presence of pinholes observed, see Supplementary Materials S3A.

Conversely, CSS-grown Sb_2Se_3 films have a rough surface morphology with exceptionally large grains in comparison to the TE films and the grains extend the full depth of the layer. Larger grains are a prerequisite for better device performance as charge mobility is faster along the Sb_2Se_3 ribbons than hopping between the ribbons (see Figures 7C,E). The CSS films also showed a degree of porosity but not to the extent observed in the TE films, Supplementary Materials S3B. The presence of pinholes in the Sb_2Se_3 films is detrimental to device performance as shunting pathways may be formed upon subsequent deposition of the Au back contact (Hutter et al., 2018b).

J-V measurements under 1-sun illumination (100 mW/cm^2) were performed on Sb_2Se_3 devices in the standard superstrate configuration and devices incorporating MoO_x and NiO HTLs. The light *J-V* curves were fitted using a single diode model to extract the values of series (R_s) and shunt (R_{sh}) resistances. Figure 8 compares the statistical distribution of the key PV parameters for these devices, where a minimum of 10 cells of each device type were measured. On average, there was a slight increase in V_{oc} when a NiO HTL was incorporated into the CSS device structure. Using a NiO HTL layer increased V_{oc} to 0.226 V from values of 0.201 and 0.186 V for Ref and MoO_x devices, respectively. The mean J_{sc} of NiO cells was also enhanced to

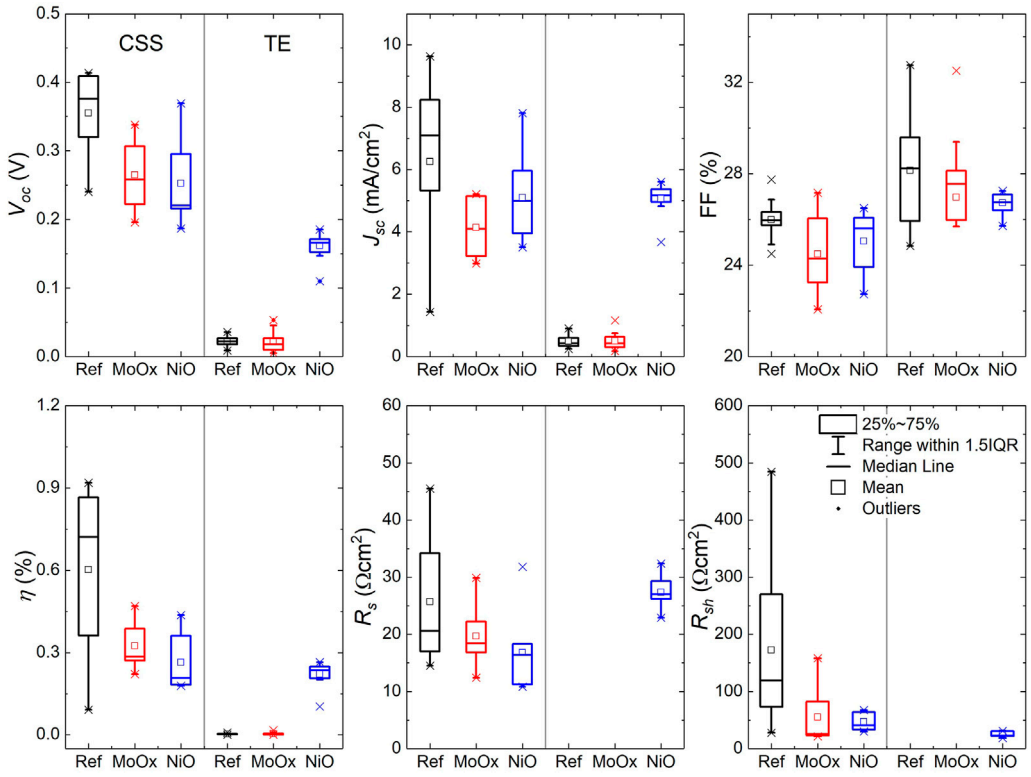

FIGURE 13
J-V parameters of substrate TE and CSS Sb_2Se_3 devices with incorporated MoO_x and NiO HTLs. □ is the average value and × is the minimum and maximum position. The three horizontal lines of each box stand for the 25%, 50% and 75% of the reading distribution. The whisker range is determined by the standard deviation of the sampled devices. IQR is the inter-quartile range.

15.94 mA/cm^2 compared to Ref (11.34 mA/cm^2) and MoO_x (10.54 mA/cm^2) cells despite a slightly lower average *FF* in the NiO devices. This translates into a higher mean NiO CSS device efficiency of 1.01% with Ref and MoO_x devices achieving efficiencies of 0.71 and 0.59% respectively. Notwithstanding the higher average R_s (2.6 Ωcm^2) and lower R_{sh} (74 Ωcm^2) values for NiO CSS solar cells compared to Ref (R_s = 2.9 Ωcm^2, R_{sh} = 119 Ωcm^2) and MoO_x (R_s = 1.3 Ωcm^2, R_{sh} = 167 Ωcm^2) cells, using NiO as a HTL increases performance by boosting J_{sc} in CSS Sb_2Se_3 superstrate devices compared to the standard and MoO_x based devices.

The average *J-V* parameters of TE Sb_2Se_3 superstrate devices followed a similar trend to those observed in the CSS devices [V_{oc}: 0.209 V (Ref) → 0.214 V (MoO_x) → 0.288 V (NiO), J_{sc}: 1.94 mA/cm^2 (MoO_x) → 8.05 mA/cm^2 (Ref) → 13.48 mA/cm^2 (NiO) ⇒ η: 0.10% (MoO_x → 0.72% (Ref) → 1.38% (NiO)]. It is worth noting that the mean *FF* of the Ref TE cells (38.0%) was higher in relation to the cells with a HTL (27.2% MoO_x, 34.6% NiO). This correlates to an increase in R_{sh} of 382 Ωcm^2 in Ref samples from R_{sh} values of 349 Ωcm^2 and 154 Ωcm^2 measured in MoO_x and NiO cells, respectively. In TE superstrate device configuration, the thin MoO_x film appears to form a more resistive layer compared to Ref and NiO devices (R_s: 10.8 Ωcm^2 MoO_x, 4.1 Ωcm^2 Ref and 6.6 Ωcm^2 NiO). Thus, overall device performance in MoO_x based solar cells is negatively impacted by low J_{sc} and high R_s which could be related to the amorphous nature of the MoO_x thin film and the presence of a current-blocking barrier at the back contact highlighted in device simulations. Despite lower *FF* in NiO based solar cells, device efficiencies exceed those of Ref and MoO_x TE devices due to improvements in V_{oc} and J_{sc} showing the benefit of using NiO as a HTL in superstrate Sb_2Se_3 solar cells.

3.4 Substrate devices

Figure 9 shows the XRD patterns of substrate Sb_2Se_3 thin films deposited *via* TE and CSS. All diffraction peaks are in good agreement with the orthorhombic Sb_2Se_3 (JCPDS 15-0861), which presents in the form of (*hk*0), (*hk*1) or (*hk*2). No diffraction peaks of other impurity phases were observed. TE Sb_2Se_3 films on Mo and Mo/MoO_x substrates show (020) and (120) peaks compared to all other Sb_2Se_3 films. The presence of (020) and (120) crystal orientations in thin Sb_2Se_3 films adversely

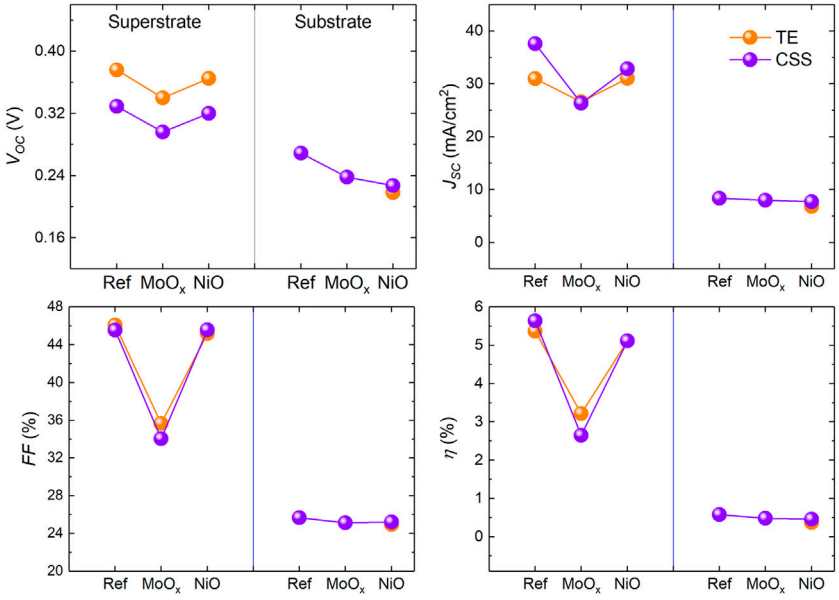

FIGURE 14
Comparison of *J-V* parameters of simulated TE and CSS Sb_2Se_3 solar cells with different HTL materials in substrate and superstrate device configurations.

affects PV device performance (Leng et al., 2014; Yuan et al., 2016; Li et al., 2017). However, when using a NiO HTL in TE Sb_2Se_3 films, it can be observed that the intensity of the diffraction peaks of Sb_2Se_3 is dominated by (221) and (211) crystal plane orientations. Furthermore, when using the Mo/NiO substrate, Sb_2Se_3 film shows an increased peak intensity for the (002) orientation. Since *h* and *k* miller indices have a zero value, it indicates that the $(Sb_4Se_6)_n$ ribbons grow perpendicular to the substrate surface (Li et al., 2019). For CSS Sb_2Se_3 films, Ref and MoO_x samples demonstrate a higher (002) peak intensity than NiO.

Figures 10, 11 show SEM images of Sb_2Se_3 films on Mo-coated SLG deposited by TE and CSS methods, respectively. The top-down SEM images of the TE films (Figures 10A–C) show a difference in morphology depending on the presence of the underlying HTL. The MoO_x sample exhibits larger Sb_2Se_3 grains than the Ref sample and the presence of pinholes in both samples is patently obvious. On the other hand, the Sb_2Se_3 grains in the NiO sample appear more angular in nature although pinholes are still present in the film. The dissimilarity in morphology is emphasised in SEM cross-section images of the TE Sb_2Se_3 films (Figures 10D–F). Voids at the absorber/Mo interface are apparent in the Ref TE sample whereas the MoO_x sample shows a homogenous film with large grains. For the NiO sample, the Sb_2Se_3 grains appear column-like with no voids at the Mo interface. The top-down SEM image of all types of CSS Sb_2Se_3 thin films (Figures 11A–C) show significantly larger grains compared to the TE films. However, Sb_2Se_3 film in the Ref sample is on average thicker (~1,000 nm) than the MoO_x (~550 nm) and NiO (~700 nm), see Figures 11D–F. The NiO sample also has a smoother surface topography.

To quantify the difference in orientations between the substrate Sb_2Se_3 thin films, the texture coefficient (TC) of diffraction peaks of the samples was calculated based on the following equation (Zoppi et al., 2006):

$$TC_{(hkl)} = \frac{\frac{I_{(hkl)}}{I_0\,(hkl)}}{\frac{1}{N}\sum_N \frac{I_{(hkl)}}{I_0\,(hkl)}} \quad (2)$$

where $I_{(hkl)}$ is the measured peak intensity of (*hkl*) plane and I_0 (*hkl*) the intensity in the standard XRD pattern. *N* is the total number of reflections considered for the calculation. A diffraction peak with a relatively large TC value (> 1) indicates a preferred orientation of the grain along this direction. Figure 12 shows the TC for Sb_2Se_3 thin films with HTLs deposited by (A) TE and (B) CSS. It is apparent from Figure 12 that NiO HTL plays a critical role in eliminating the detrimental (*hk*0) planes in the TE samples and at the same time, significantly increases absorber growth in planes, i.e., (211), (221) that are perpendicular to the substrate surface. This further supports the enhanced device performance in solar cells when NiO is used as the HTL. In CSS samples, this templating effect of HTLs is not observed as no (*hk*0) planes are grown in the Ref and MoO_x samples. MoO_x increases the growth of favoured crystal planes including (211), (221), and (002) compared to the Ref substrate sample whereas NiO appears to inhibit the growth of the preferential planes, which may be attributed to rendering the seed layer ineffective but further study will be required to fully understand the reason.

Figure 13 shows the variation in *J-V* parameters measured for a minimum batch size of 10 Sb_2Se_3 solar cells in substrate configuration deposited by TE and CSS incorporating HTLs. The use of MoO_x/NiO HTLs adversely affects all device parameters in CSS-based solar cells. This can be explained by lower average R_{sh} values of 55 Ωcm^2 and 47 Ωcm^2 determined for MoO_x and NiO device types, respectively, compared to 172 Ωcm^2 in the Ref devices. The reason for the reduction in R_{sh} of the substrate devices with a HTL is not obvious. Only working TE devices were achieved by incorporating a NiO HTL, which can be attributed to the templating effect of the NiO film which eliminated the deleterious (*hk*0) crystal planes and promoted the growth of preferred (211) and (221) planes. As highlighted in device simulations, the performance of substrate Sb_2Se_3 solar cells can be dependent on the WF of Mo back contact (see Figure 3). Mo metal typically has a WF in the range of 4.5–4.95 eV. KPFM measurements on Mo coated SLG prior to Sb_2Se_3 deposition determined the Mo WF to be 4.6 eV. According to simulations, device performance of Ref and MoO_x substrate devices is severely impacted at the observed Mo WF. Simulated NiO device performance is affected to a lesser degree.

R_s values for both TE and CSS substrate Sb_2Se_3 devices were significantly higher than their superstrate counterparts and had a detrimental effect on overall substrate device performance. This could be related to a non-optimal sputtered ITO layer in the substrate devices with a typical sheet resistance of ~ 35 Ω/□ (Qu et al., 2016) compared to commercially available ITO-coated glass slides used in superstrate devices with sheet resistances of 8–12 Ω/□ (Sigma Aldrich).

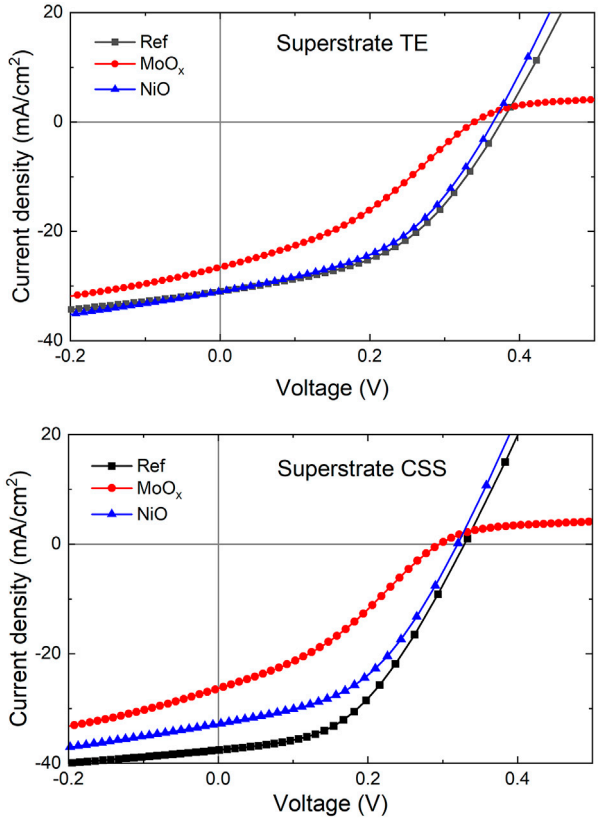

FIGURE 15
J-V curves for simulated TE and CSS Sb_2Se_3 devices with HTLs in superstrate configuration. Roll-over behaviour is evident in both TE and CSS devices with MoO_x HTL indicating a carrier transport barrier at the back contact.

3.5 Simulated and fabricated device comparison

Experimentally determined device parameters, such as R_s and R_{sh} and apparent doping density (N_A) of the Sb_2Se_3 absorber, were incorporated into SCAPS simulations of TE/CSS Sb_2Se_3 devices in superstrate/substrate configurations in order to replicate the observed behaviour of the fabricated devices. For an accurate representation of the fabricated cells, the N_A value for the Sb_2Se_3 absorber in the CSS devices was set to a value previously determined for the same CSS deposition process used in this study with a Sb_2Se_3 absorber thickness of 1 μm (Phillips et al., 2019). An experimentally determined N_A value for a typical 500 nm thick TE Sb_2Se_3 absorber was used in TE device simulations (see Table 1 for TE/CSS Sb_2Se_3 film properties). Figure 14 shows device performance of the simulated TE/CSS Sb_2Se_3 devices with experimentally determined R_s, R_{sh} and N_A values. Similar trends are observed for all device parameters of the simulated and fabricated solar cells in both device configurations indicating the simulated devices are a reasonable representation of actual Sb_2Se_3 solar cells (see Figures 8, 13). However, in superstrate configuration, simulations overestimate all *J-V* parameters, indicating factors other than R_s, R_{sh} and N_A are influencing device performance. Material properties such as carrier lifetimes, defects and band tails states have been cited as having a detrimental effect on overall device performance (Chen and Tang, 2020). In that work, a number of bulk defects in Sb_2Se_3 were identified with energy levels within the Sb_2Se_3 bandgap ranging from 0.18–0.94 eV above the valence band maximum. For simulation purposes, a mid-gap donor defect (0.62 eV) was introduced for the Sb_2Se_3 bulk to reproduce realistic device performance (Wen et al., 2018; Ma et al., 2020). Chen and Tang (2020) also highlighted significant recombination occurring at the *n-p* interface which severely impacts both V_{oc} and J_{sc}. The presence of additional Sb_2Se_3 bulk defects and increased absorber/buffer interface defect concentration could account for the differences observed between the simulated and fabricated devices studied here.

TABLE 1 Device simulation parameters, d: layer thickness, E_g: bandgap, χ: electron affinity, $\varepsilon/\varepsilon_0$: dielectric constant, $N_{C/V}$: effective density of states C: conduction band (CB) V: valence band (VB), $\mu_{e,h}$: carrier mobility, $N_{A/D}$: apparent doping density D: donor A: acceptor, $\sigma_{e,h}$: capture cross section, N_{int}: interface defect concentration, E_t: defect energy level relative to CB/VB and N_{bulk}: bulk defect concentration. Subscripts e and h are electron and hole, respectively.

Properties	MoO_x	NiO	Sb_2Se_3	CdS	*i*-ZnO	ITO
d (nm)	15	15	500 (TE). 1,000 (CSS)	70	35	200
E_g (eV)	3.85[a]	3.95[a]	1.17[a]	2.72[a]	3.37[b]	3.72[c]
χ (eV)	2.20[e]	1.46[f]	4.15[g]	4.70[c]	4.70[c]	4.50[days]
$\varepsilon/\varepsilon_0$	10.0[e]	11.9[f]	14.4[g]	9.0[b]	9.0[b]	9.4[days]
N_C (cm^{-3})	2.2×10^{18}[e]	2.2×10^{18}[f]	2.2×10^{18}[g]	2.1×10^{18}[b]	1.8×10^{19}[b]	4.0×10^{19}[c]
N_V (cm^{-3})	1.8×10^{19}[e]	1.8×10^{19}[f]	1.8×10^{19}[g]	1.7×10^{19}[b]	2.4×10^{18}[b]	1.0×10^{18}[c]
μ_e (cm^2/Vs.)	30[e]	2.8[f]	100[g]	160[b]	200[b]	30[b]
μ_h (cm^2/Vs.)	2.5[e]	2.8[f]	25[g]	15[b]	93[b]	5[b]
$N_{A/D}$ (cm^{-3})	D:3 × 10^{16}[e]	A:3 × 10^{18}[f]	A:1 × 10^{14}[h] (TE). A:1 × 10^{16}[i] (CSS)	D:1 × 10^{17}[b]	D:1 × 10^{18}[b]	D:1 × 10^{21}[b]
Defects at Sb_2Se_3/CdS interface (Gaussian distribution throughout interface)						
N_{int} (cm^{-3})			D: varied	A: varied		
σ_e (cm^2)			10^{-13}	10^{-15}		
σ_h (cm^2)			10^{-15}	10^{-13}		
Bulk Sb_2Se_3 defects (Gaussian distribution throughout bulk)						
N_{bulk} (cm^{-3})			D: 2.6 × 10^{16}[j]	A: 5.0 × 10^{15}[b]		
E_t (eV)			0.62[j]	1.20[b]		
σ_e (cm^2)			10^{-13}	10^{-17}		
σ_h (cm^2)			10^{-15}	10^{-13}		

[a]Experimentally determined from UV-VIS, measurements.
[b]Reference (Kanevce et al., 2015).
[c]Reference (Erkan et al., 2016).
[d]Reference (Kartopu et al., 2019).
[e]Reference (Ni et al., 2019).
[f]Reference (Casas et al., 2017).
[g]Reference (Maurya and Singh, 2021).
[h]Experimentally determined from capacitance-voltage *C-V* measurements.
[i]Reference (Phillips et al., 2019).
[j]Reference (Chen and Tang, 2020).

In addition, it is worth noting actual superstrate devices which incorporate a MoO_x HTL under-perform in relation to standard simulated superstrate devices (see Figure 8). This decrease in performance is not observed in the fabricated substrate Sb_2Se_3 solar cells with a MoO_x HTL. This discrepancy can be accounted for by different processing conditions applied during deposition of substrate and superstrate devices. During deposition of Sb_2Se_3 layer on SLG/Mo/HTL substrate, the substrate temperature is maintained at 300°C which is sufficient to crystallise the MoO_x film, see Supplementary Materials S4. The crystallised MoO_x film consists of a mixture of MoO_2, MoO_3 and intermediate reduced oxide phases. The phase composition affects the electronic and optical properties of the MoO_x film, with MoO_2 content lowering the resistivity, transmittance and bandgap (Inzani et al., 2017). Simulations also show a roll-over in the *J-V* curves for superstrate Sb_2Se_3 devices in both configurations (see Figure 15), indicating the presence of a barrier to carrier transport at the back contact seen in simulated energy band alignments as previously discussed (Figure 4).

4 Conclusion

Numerical simulations of standard planar superstrate and substrate Sb_2Se_3 solar cells along with the effect of incorporating MoO_x and NiO HTLs, demonstrated an increase in device efficiency for cells with a HTL which was achieved by an increase in J_{sc} for both substrate and superstrate device configurations. Both HTLs have high bandgaps and low electron affinities compared to Sb_2Se_3 absorber which manifests as a large barrier for electrons at the metallic back electrode and facilitates hole extraction. However, a roll-over effect was seen in the simulated *J-V* curve of the substrate device with MoO_x HTL, suggesting a current-blocking barrier at the back contact caused by non-optimal energy band alignment. Material characterisation of the HTL materials deposited by E-beam evaporation at room temperature revealed MoO_x formed an amorphous layer while NiO crystallised in cubic crystal orientation. 15 nm thick HTLs were incorporated into superstrate/substrate solar cells with

Sb_2Se_3 absorbers deposited by thermal evaporation and close-space sublimation. For CSS superstrate solar cells with NiO HTL, device efficiency was enhanced by a 40% increase in J_{sc} compared to reference and MoO_x based devices. TE superstrate cells incorporating NiO as HTL also demonstrated improved efficiencies achieved by higher V_{oc} and J_{sc}. In the superstrate TE cells with MoO_x HTL, J_{sc} was severely inhibited which is attributed to MoO_x forming a more resistive layer due to its amorphous nature. Conversely, the presence of a MoO_x or NiO HTL in substrate CSS-deposited Sb_2Se_3 solar cells reduced device performance which is linked to lower average R_{sh} observed in these cells. Optimisation of HTL thickness and/or re-optimisation of the absorber deposition could potentially alleviate this issue. Simulations reveal a connection between the WF of the Mo metal back contact and substrate device performance. For an experimentally determined Mo WF of 4.6 eV, all device *J-V* characteristics are significantly reduced, whereas substrate devices with NiO HTL are only marginally affected. In addition, XRD analysis of TE Sb_2Se_3 films with NiO HTL revealed a templating effect on Sb_2Se_3 crystal orientation where detrimental (020)/(120) crystal planes were eliminated and preferred (211)/(221) planes increased in intensity which resulted in increased device performance of substrate Sb_2Se_3 solar cells. NiO shows more promise as a HTL in Sb_2Se_3 PV devices, and crucially can act as a templating layer when the Sb_2Se_3 deposition method does not already impart the desired structure, as is often the case with TE devices.

Data availability statement

Data is available *via* this link: https://figshare.com/projects/Routes_to_Increase_Performance_for_Antimony_Selenide_Solar_Cells_using_Inorganic_Hole_Transport_Layers/140140.

Author contributions

SC, RV, LP, and JM fabricated absorbers and solar cells, SC conducted material and device characterisation, data analysis and device simulations. SC wrote the manuscript with contribution from OH. OH, YQ, VB, NB, and GZ discussed results and contributed to manuscript mofification and finalisation. VB and YQ supervised the project.

Acknowledgments

The authors acknowledge the EPSRC Centre for Doctoral Training in Renewable Energy Northeast Universities (ReNU) for funding through grant EP/S023836/1. The authors also appreciate the support from North East Centre for Energy Materials (NECEM) (EP/R021503/1) and British Council Newton Fund Institutional Links Grant in Ultralight Absorber for Remote Energy Source (U-AREs, No. 623804307). Discussions regarding NiO thin film deposition with Prof. Elizabeth Gibson, School of Natural and Environmental Sciences, Newcastle University is acknowledged.

Conflict of interest

The authors declare that the research was conducted in the absence of any commercial or financial relationships that could be construed as a potential conflict of interest.

Publisher's note

Supplementary material

The Supplementary Material for this article can be found online at: https://www.frontiersin.org/articles/10.3389/fchem.2022.954588/full#supplementary-material

References

Birkett, M., Linhart, W. M., Stoner, J., Phillips, L. J., Durose, K., Alaria, J., et al. (2018). Band gap temperature-dependence of close-space sublimation grown Sb_2Se_3 by photo-reflectance. *Apl. Mater.* 6, 084901. doi:10.1063/1.5027157

Black, J., Conwell, E., Seigle, L., and Spencer, C. (1957). Electrical and optical properties of some M2v–bN3vi–b semiconductors semiconductors. *J. Phys. Chem. Solids* 2, 240–251. doi:10.1016/0022-3697(57)90090-2

Burgelman, M., Nollet, P., and Degrave, S. (2000). Modelling polycrystalline semiconductor solar cells. *Thin Solid Films* 361-362, 527–532. doi:10.1016/S0040-6090(99)00825-1

Casas, G., Cappelletti, M., Cédola, A., Soucase, B. M., and Peltzer y Blancá, E. (2017). Analysis of the power conversion efficiency of perovskite solar cells with different materials as Hole-Transport Layer by numerical simulations. *Superlattices Microstruct.* 107, 136–143. doi:10.1016/j.spmi.2017.04.007

Chen, C., Bobela, D. C., Yang, Y., Lu, S., Zeng, K., Ge, C., et al. (2017). Characterization of basic physical properties of Sb_2Se_3 and its relevance for photovoltaics. *Front. Optoelectron.* 10, 18–30. doi:10.1007/s12200-017-0702-z

Chen, C., Li, W., Zhou, Y., Chen, C., Luo, M., Liu, X., et al. (2015). Optical properties of amorphous and polycrystalline Sb_2Se_3 thin films prepared by thermal evaporation. *Appl. Phys. Lett.* 107, 043905. doi:10.1063/1.4927741

Chen, C., and Tang, J. (2020). Open-circuit voltage loss of antimony chalcogenide solar cells: Status, origin, and possible solutions. *ACS Energy Lett.* 5, 2294–2304. doi:10.1021/acsenergylett.0c00940

Deringer, V. L., Stoffel, R. P., Wuttig, M., and Dronskowski, R. (2015). Vibrational properties and bonding nature of Sb_2Se_3 and their implications for chalcogenide materials. *Chem. Sci.* 6, 5255–5262. doi:10.1039/C5SC00825E

Eisenbarth, T., Caballero, R., Nichterwitz, M., Kaufmann, C. A., Schock, H.-W., and Unold, T. (2011). Characterization of metastabilities in Cu(In, Ga)Se_2 thin-film solar cells by capacitance and current-voltage spectroscopy. *J. Appl. Phys.* 110, 094506. doi:10.1063/1.3656453

Erkan, M. E., Chawla, V., and Scarpulla, M. A. (2016). Reduced defect density at the CZTSSe/CdS interface by atomic layer deposition of Al_2O_3. *J. Appl. Phys.* 119, 194504. doi:10.1063/1.4948947

Fleck, N., Hutter, O. S., Phillips, L. J., Shiel, H., Hobson, T. D. C., Dhanak, V. R., et al. (2020). How oxygen exposure improves the back contact and performance of antimony selenide solar cells. *ACS Appl. Mat. Interfaces* 12, 52595–52602. doi:10.1021/acsami.0c14256

Green, M. (1969). Solid state surface science volume 1. *J. Macromol. Sci. Part B* 3, 366. doi:10.1080/00222346908205102

Guo, L., Zhang, B., Qin, Y., Li, D., Li, L., Qian, X., et al. (2018). Tunable quasi-one-dimensional ribbon enhanced light absorption in Sb_2Se_3 thin-film solar cells grown by close-space sublimation. *Sol. RRL* 2, 1800128. doi:10.1002/solr.201800128

Hädrich, M., Heisler, C., Reislöhner, U., Kraft, C., and Metzner, H. (2011). Back contact formation in thin cadmium telluride solar cells. *Thin Solid Films* 519, 7156–7159. doi:10.1016/j.tsf.2010.12.144

Hölzl, J., and Schulte, F. K. (1979). "Work function of metals," in *Solid surface physics*. 2nd Edn, Editor J. Hölzl, F.K. Schulte, and H. Wagner (Berlin, Heidelberg: Springer), vol. 85, 1–150.

Hutter, O. S., Phillips, L. J., Durose, K., and Major, J. D. (2018a). 6.6% efficient antimony selenide solar cells using grain structure control and an organic contact layer. *Sol. Energy Mater. Sol. Cells* 188, 177–181. doi:10.1016/j.solmat.2018.09.004

Hutter, O. S., Phillips, L. J., Yates, P. J., Major, J. D., and Durose, K. (2018b). "CSS antimony selenide film morphology and high efficiency PV devices," in 2018 IEEE 7th World Conference on Photovoltaic Energy Conversion (WCPEC)(A Joint Conference of 45th IEEE PVSC, 28th PVSEC & 34th EU PVSEC) (IEEE).

Inzani, K., Nematollahi, M., Vullum-Bruer, F., Grande, T., Reenaas, T. W., and Selbach, S. M. (2017). Electronic properties of reduced molybdenum oxides. *Phys. Chem. Chem. Phys.* 19, 9232–9245. doi:10.1039/C7CP00644F

Kanevce, A., Repins, I., and Wei, S.-H. (2015). Impact of bulk properties and local secondary phases on the $Cu_2(Zn, Sn)Se_4$ solar cells open-circuit voltage. *Sol. Energy Mater. Sol. Cells* 133, 119–125. doi:10.1016/j.solmat.2014.10.042

Kartopu, G., Williams, B., Zardetto, V., Gürlek, A., Clayton, A., Jones, S., et al. (2019). Enhancement of the photocurrent and efficiency of CdTe solar cells suppressing the front contact reflection using a highly-resistive ZnO buffer layer. *Sol. Energy Mater. Sol. Cells* 191, 78–82. doi:10.1016/j.solmat.2018.11.002

Leijtens, T., Eperon, G. E., Barker, A. J., Grancini, G., Zhang, W., Ball, J. M., et al. (2016). Carrier trapping and recombination: The role of defect physics in enhancing the open circuit voltage of metal halide perovskite solar cells. *Energy Environ. Sci.* 9, 3472–3481. doi:10.1039/c6ee01729k

Leng, M., Luo, M., Chen, C., Qin, S., Chen, J., Zhong, J., et al. (2014). Selenization of Sb_2Se_3 absorber layer: An efficient step to improve device performance of CdS/Sb_2Se_3 solar cells. *Appl. Phys. Lett.* 105, 083905. doi:10.1063/1.4894170

Li, Z., Chen, X., Zhu, H., Chen, J., Guo, Y., Zhang, C., et al. (2017). Sb_2Se_3 thin film solar cells in substrate configuration and the back contact selenization. *Sol. Energy Mater. Sol. Cells* 161, 190–196. doi:10.1016/j.solmat.2016.11.033

Li, Z., Liang, X., Li, G., Liu, H., Zhang, H., Guo, J., et al. (2019). 9.2%-efficient core-shell structured antimony selenide nanorod array solar cells. *Nat. Commun.* 10, 125. doi:10.1038/s41467-018-07903-6

Liu, X., Chen, J., Luo, M., Leng, M., Xia, Z., Zhou, Y., et al. (2014). Thermal evaporation and characterization of Sb_2Se_3 thin film for substrate Sb_2Se_3/CdS solar cells. *ACS Appl. Mat. Interfaces* 6, 10687–10695. doi:10.1021/am502427s

Ma, Y., Tang, B., Lian, W., Wu, C., Wang, X., Ju, H., et al. (2020). Efficient defect passivation of Sb_2Se_3 film by tellurium doping for high performance solar cells. *J. Mat. Chem. A* 8, 6510–6516. doi:10.1039/D0TA00443J

Maurya, K., and Singh, V. (2021). Sb_2Se_3 versus Sb_2S_3 solar cell: A numerical simulation. *Sol. Energy* 228, 540–549. doi:10.1016/j.solener.2021.09.080

Michaelson, H. B. (1977). The work function of the elements and its periodicity. *J. Appl. Phys.* 48, 4729–4733. doi:10.1063/1.323539

Ni, M., Liu, J.-M., Li, Z.-Q., Shen, Q., Feng, Y.-Z., and Feng, X.-D. (2019). Simulation of graded bandgap on backwall superstrate CIGS solar cells with MoO_x electron reflection layer. *Mat. Res. Express* 6, 116441. doi:10.1088/2053-1591/ab4c5c

Phillips, L. J., Savory, C. N., Hutter, O. S., Yates, P. J., Shiel, H., Mariotti, S., et al. (2019). Current enhancement via a TiO_2 window layer for CSS Sb_2Se_3 solar cells: Performance limits and high V_{oc}. *IEEE J. Photovolt.* 9, 544–551. doi:10.1109/jphotov.2018.2885836

Qu, Y., Zoppi, G., and Beattie, N. S. (2016). The role of nanoparticle inks in determining the performance of solution processed $Cu_2ZnSn(S, Se)_4$ thin film solar cells. *Prog. Photovolt. Res. Appl.* 24, 836–845. doi:10.1002/pip.2756

Tauc, J., Grigorovici, R., and Vancu, A. (1966). Optical properties and electronic structure of amorphous germanium. *Phys. Stat. Sol.* 15, 627–637. doi:10.1002/pssb.19660150224

Wang, L., Li, D.-B., Li, K., Chen, C., Deng, H.-X., Gao, L., et al. (2017). Stable 6%-efficient Sb_2Se_3 solar cells with a ZnO buffer layer. *Nat. Energy* 2, 17046. doi:10.1038/nenergy.2017.46

Wang, Y., Xia, Z., Liang, J., Wang, X., Liu, Y., Liu, C., et al. (2015). Towards printed perovskite solar cells with cuprous oxide hole transporting layers: A theoretical design. *Semicond. Sci. Technol.* 30, 054004. doi:10.1088/0268-1242/30/5/054004

Wen, X., Chen, C., Lu, S., Li, K., Kondrotas, R., Zhao, Y., et al. (2018). Vapor transport deposition of antimony selenide thin film solar cells with 7.6% efficiency. *Nat. Commun.* 9, 2179. doi:10.1038/s41467-018-04634-6

Williams, R. E., Ramasse, Q. M., McKenna, K. P., Phillips, L. J., Yates, P. J., Hutter, O. S., et al. (2020). Evidence for self-healing benign grain boundaries and a highly defective Sb_2Se_3–cds interfacial layer in Sb_2Se_3 thin-film photovoltaics. *ACS Appl. Mat. Interfaces* 12, 21730–21738. PMID: 32314567. doi:10.1021/acsami.0c03690

Yuan, C., Zhang, L., Liu, W., and Zhu, C. (2016). Rapid thermal process to fabricate Sb_2Se_3 thin film for solar cell application. *Sol. Energy* 137, 256–260. doi:10.1016/j.solener.2016.08.020

Zeng, K., Xue, D.-J., and Tang, J. (2016). Antimony selenide thin-film solar cells. *Semicond. Sci. Technol.* 31, 063001. doi:10.1088/0268-1242/31/6/063001

Zhou, Y., Wang, L., Chen, S., Qin, S., Liu, X., Chen, J., et al. (2015). Thin-film Sb_2Se_3 photovoltaics with oriented one-dimensional ribbons and benign grain boundaries. *Nat. Photonics* 9, 409–415. doi:10.1038/nphoton.2015.78

Zoppi, G., Durose, K., Irvine, S. J. C., and Barrioz, V. (2006). Grain and crystal texture properties of absorber layers in MOCVD-grown CdTe/CdS solar cells. *Semicond. Sci. Technol.* 21, 763–770. doi:10.1088/0268-1242/21/6/009